Research Article

Fengjie Cui, Shaoxian Gu, Ningyu Wang, Chuou Yin, Shengyuan Zhang, Jinyou Hu, Yunzhu Cai, Zhangwen Wu, Chengjun Gou, and Jun Wang*

Hybrid pencil beam model based on photon characteristic line algorithm for lung radiotherapy in small fields

https://doi.org/10.1515/phys-2022-0194
received January 09, 2022; accepted August 07, 2022

Abstract: Hybrid pencil beam model (HPBM) based on photon characteristic line algorithm has been presented to get accurate three-dimensional (3D) dose distribution for lung radiotherapy in small fields. In the model, we introduced a scattering factor to accurately describe the transport behavior of scattered photons and secondary electrons, combined with the equivalent depth correction and the weighted density correction. The pencil beam kernels of heterogeneous lung phantoms were redefined by the scattering factor and depth dose for a reference field by photon characteristic line algorithm. Subsequently, the 3D dose distribution in lung phantoms with density of 0.1, 0.26, and 0.4 g/cm^3, was calculated by the Finite-size pencil beam algorithm in five regular fields and an irregular field for 6 MV photon beam. The dose distributions obtained by the HPBM are in agreement with those obtained by the MC simulations, with a relative error of less than 3% in most of the cases. However, there are apparent discrepancies at media interfaces and lung anterior portion. Moreover, at media interfaces, relative dose errors of the two methods decrease with the increase in field size and lung density. The depth range in which relative errors is greater than 3% increases with the increase in field size at lung anterior portion. In these examples, maximum relative errors are between 5 and 29%. Nevertheless, it is shown that the HPBM based on photon characteristic line algorithm has potential research values in lung dose calculation under conditions of small fields.

Keywords: hybrid pencil beam model based on photon characteristic line algorithm, Monte Carlo simulation, small fields, lung phantom

1 Introduction

With the development of various radiotherapy technologies, such as intensity modulated radiation therapy, and stereotactic radiation therapy, the accuracy of treatment planning system (TPS) could achieve submillimeter level. In these techniques, multi-leaf collimators are used to form small and irregular fields to ensure maximum consistency between the high dose deposition region and the tumor spatial anatomical shape [1–4]. Thus, the tumor control probability can be improved and the normal tissue complication probability can be reduced. International Commission Radiological Units Report No. 24 proposes that the dose algorithm error in clinical TPS should be kept within 3% [5]. However, many studies indicate that the phenomenon of charged particle nonequilibrium becomes more pronounced with the decrease in field size, density of heterogeneous tissue, and increase in the incident photon energy for small fields (the field size is smaller than the maximum range of secondary electron transport). Especially in radiotherapy of lung tumor, lung density changes are more likely to cause lack of charged particle equilibrium (CPE) [6–9]. In fact, the existence of multi-factor makes the lung dose calculations more intricate and inaccurate. American Association of Physicists in Medicine No. 24 proposes that low-energy beams are preferred in irradiating lung tumors, because higher

* **Corresponding author: Jun Wang,** Key Laboratory of Radiation Physics and Technology of Ministry of Education, Institute of Nuclear Science and Technology, Sichuan University, Chengdu, 610064, China, e-mail: wangjun@scu.edu.cn
Fengjie Cui, Shaoxian Gu, Ningyu Wang, Chuou Yin, Shengyuan Zhang, Yunzhu Cai, Zhangwen Wu, Chengjun Gou: Key Laboratory of Radiation Physics and Technology of Ministry of Education, Institute of Nuclear Science and Technology, Sichuan University, Chengdu, 610064, China
Jinyou Hu: Key Laboratory of Radiation Physics and Technology of Ministry of Education, Institute of Nuclear Science and Technology, Sichuan University, Chengdu, 610064, China; Cancer Center, Sichuan Academy of Medical Sciences & Sichuan Provincial People's Hospital, Chengdu, 610072, China

energy beams would need larger field margins to achieve target dose homogeneity. For 6 MV photon beam widely used in TPS, the radiation field with a size less than 3 cm × 3 cm is considered as small field [10]. The accurate radiotherapy algorithm for lung radiotherapy in small fields is one of the research hotspots.

At present, many dose algorithms are used for lung dose calculation in small fields in clinic, such as pencil beam convolution (PBC), Acuros XB, and anisotropic analytical algorithms [11,12]. As the most accurate dose algorithm, MC method, which is based on the probability and statistics theory, simulates the random process of particles transport. However, it failed to be used in TPS because of its time-consuming computation [13,14]. In recent years, the pencil beam is increasingly used to accurately describe the influence of heterogeneous tissue on dose distribution. And those influence can be described by correcting pencil beam kernel of homogeneous media, which can be directly expressed by simulating pencil beam data.

In this work, Hybrid pencil beam model (HPBM) is presented to get accurate three-dimensional (3D) dose distribution for lung radiotherapy in small fields. In the algorithm, the fluence distributions of energetic photons and secondary electrons are described by photon characteristic line algorithm under the condition of infinitely broad beam, and the accurate dose distribution of central axis can be obtained. The 3D pencil beam kernel of pure water phantom, as pre-stored data, is calculated by MC method. The pencil beam kernel of the lung phantom is obtained by the heterogeneous correction on the basis of the pencil beam kernel of water phantom. And then, using the accurate depth dose distribution of the lung phantom obtained by the photon characteristic line algorithm in a broad beam, we redefine lung phantom pencil beam kernel and use it for calculating the 3D dose distribution in lung phantom for any radiation fields by Finite-size pencil beam (FSPB) algorithm. Finally, the calculated results are compared with MC simulation data to verify the HPBM algorithm precision.

2 Methods

2.1 Monte Carlo simulations

In this study, the dose distribution in lung phantoms with different density was simulated by the MC software EGSnrc/Dosxyznrc, in various radiation fields for 6 MV photon beam. The global electron and photon cutoff energies were 0.521 and 0.01 MeV, respectively [15,16]. The electron-step and boundary crossing algorithms were PRESTA-II and EXACT, respectively. The parallel rectangular beam was used as the photon source type. The energy spectrum data file was mohan6.spectrum. The statistical error was controlled within 1% in the whole simulation process.

We simulated a pure water phantom and a water–lung–water phantom of the same size, with the origin of coordinate at the surface center. The lung phantom dimension was $40 \times 40 \times (d_1 + d_2 + d_3)$ cm^3. d_1, d_2 and d_3 were, respectively, 10, 10, and 20 cm, representing the thickness of the chest wall of the anterior lung tissue, the thickness of lung tissue, and the thickness of the chest wall of the posterior lung tissue. The chest wall can be considered as resembling water tissue. Elemental composition and proportion of water and lung tissue were derived from the Dosxyznrc material library file (521cru.pegs4dat). The voxel size was 0.25 cm × 0.25 cm × 0.25 cm and the pencil beam size was 0.25 cm × 0.25 cm. Here three lung densities of 0.1, 0.26, and 0.4 g/cm^3 were considered, respectively.

2.2 HPBM

The interaction between photons and body tissues takes place *via* three main ways, namely, photoelectric effect, Compton scattering, and electron pair effect. The total micro cross section of these interactions was expressed as

$$\sigma_{\text{tot}} = \sigma_{\text{pe}} + \sigma_{\text{comp}} + \sigma_{\text{pair}}, \tag{1}$$

where σ_{pe}, σ_{comp}, and σ_{pair} are micro cross sections of photoelectric effect, Compton scattering, and electron pair effect, respectively. When the infinitely broad beam with energy of E_0 is vertically incident upon the surface of the medium, the photon transport in homogeneous medium generally started with the Boltzmann equation

$$\begin{cases} \mu \dfrac{\partial \varnothing}{\partial z} = -\sum(z, E)\varnothing(z, E, \mu) \\ + \displaystyle\int_{4\pi} \mathrm{d}\Omega' \int_{E}^{E_0} \mathrm{d}E' \varnothing(z, E', \Omega') K(z, E' \to E, \Omega' \to \Omega) \\ + S(z, E, \mu) \\ S(z, E, \mu) = \delta(z)\delta(E - E_0)\delta(1 - \mu)/2\pi \end{cases}, \tag{2}$$

where $\varnothing(z, E, \mu)$ is the photon differential fluence distribution, $\varnothing(z, E, \mu)\mathrm{d}E\mathrm{d}\mu$ is the photon fluence at depth of z with energies between E and $E + \mathrm{d}E$, and directions between μ and $\mu + \mathrm{d}\mu$. $K(z, E' \to E, \Omega' \to \Omega)\mathrm{d}E'\mathrm{d}\Omega'$ is

the probability of a photon with energy E' and direction Ω' passing through a medium with a unit mass thickness at depth z. $S(z, E, \mu)$ is the source term. $\sum(z, E)$ is the linear attenuation coefficient of photons with energy E at depth z, and then we can write

$$\sum(z, E) = n_{(z)} \cdot \sigma_{\text{tot}}(z, E), \tag{3}$$

where

$$n_{(z)} = \frac{N_{\text{A}}}{A_{(z)}} \cdot \rho_{(z)}, \tag{4}$$

where N_{A} is the Avogadro constant. $A_{(z)}$ is the atomic mass of the medium at depth z. $\rho_{(z)}$ is the density of the medium at depth z.

In the photon characteristic line algorithm [17,18], the photon fluence was given by

$$\varnothing(z, E, \mu) = \varnothing_0(z, E, \mu) + \varnothing_1(z, E, \mu) + \varnothing_m(z, E, \mu), \tag{5}$$

where $\varnothing_0(z, E, \mu)$, $\varnothing_1(z, E, \mu)$, $\varnothing_m(z, E, \mu)$ are uncollided photon beam, single scattered photon beam, and multiple scattered photon beam, respectively. The transport equation of uncollided photon beam was expressed as [17,18]

$$\begin{aligned} &\mu\frac{\partial\varnothing_0(z, E, \mu)}{\partial z} + \sum(z, E)\varnothing_0(z, E, \mu) \\ &\quad = \frac{\delta(z)\delta(1-\mu)\delta(E-E_0)}{2\pi}. \end{aligned} \tag{6}$$

The transport equation of single scattered photon beam was expressed as [17,18]

$$\begin{cases} \mu\dfrac{\partial\varnothing_1(z, E, \mu)}{\partial z} + \sum(z, E)\varnothing_1(z, E, \mu) = S_1(z, E, \mu) \\ S_1(z, E, \mu) = \displaystyle\int_{4\pi} \mathrm{d}\mu' \int_{\lambda}^{\lambda-2} \mathrm{d}E'\varnothing_0(z, E', \mu')K(z, E' \\ \qquad \to E, \Omega' \to \Omega)\dfrac{\delta(\mu\mu' - 1 - \lambda' + \lambda)}{2\pi}. \end{cases} \tag{7}$$

The transport equation of multiple scattered photon beam was expressed as [17,18]

$$\begin{cases} \mu\dfrac{\partial\varnothing_m(z, E, \mu)}{\partial z} + \sum(z, E)\varnothing_1(z, E, \mu) = S(z, E, \mu) \\ S(z, E, \mu) = S_2(z, E, \mu) + S_m(z, E, \mu) \\ S_2(z, E, \mu) = \displaystyle\int_{4\pi} \mathrm{d}\mu' \int_{\lambda}^{\lambda-2} \mathrm{d}E'\varnothing_1(z, E', \mu')K(z, E' \to E, \Omega' \\ \qquad \to \Omega)\dfrac{\delta(\mu\mu' - 1 - \lambda' + \lambda)}{2\pi} \\ S_m(z, E, \mu) = \displaystyle\int_{4\pi} \mathrm{d}\mu' \int_{\lambda}^{\lambda-2} \mathrm{d}E'\varnothing_m(z, E', \mu')K(z, E' \to E, \Omega' \\ \qquad \to \Omega)\dfrac{\delta(\mu\mu' - 1 - \lambda' + \lambda)}{2\pi}. \end{cases} \tag{8}$$

In Eqs. (7) and (8), λ is expressed as

$$\lambda = \frac{m_0c^2}{E}. \tag{9}$$

$\varnothing_0(z, E, \mu)$, $\varnothing_1(z, E, \mu)$ have explicit analytic solutions, and $\varnothing_m(z, E, \mu)$ can only get the numerical solution by numerical methods. The direction cosine μ can be discretized according to the direction of characteristic lines while calculating the numerical solutions of $\varnothing_m(z, E, \mu)$. Then, the solution of Eq. (7) is [17,18]

$$\varnothing_0(z, E, \mu) = \frac{\delta(1-\mu)\delta(E-E_0)}{2\pi}\mathrm{e}^{-\sum(z,E_0)z}. \tag{10}$$

The solution of Eq. (8) is [17,18]

$$\begin{cases} \varnothing_1(z, E, \mu) = A_1 \cdot \begin{cases} \mathrm{e}^{-\sum(z,E_0)z} - \mathrm{e}^{\frac{-\sum(z,E)z}{\mu}}, & (\mu \ge 0) \\ \mathrm{e}^{-\sum(z,E_0)z} - \mathrm{e}^{\frac{-\sum(z,E)(d-z)}{\mu}}, & (\mu < 0) \end{cases} \\ A_1 = \dfrac{\delta(\mu - 1 - \lambda_0 + \lambda)K(z, E' \to E, \Omega' \to \Omega)}{2\pi(\sum(z, E) - \mu\sum(z, E_0))}. \end{cases} \tag{11}$$

The solution of Eq. (9) is [17,18]

$$\begin{aligned} &\varnothing_m(z, E, \mu) \\ &= \begin{cases} \mathrm{e}^{\left(-\frac{-\sum(z,E)Z}{\mu}\right)}\displaystyle\int_0^z \mathrm{d}z', \dfrac{S(z', E, \mu)}{\mu}\mathrm{e}^{\left(-\frac{-\sum(z,E)z'}{\mu}\right)}, & (\mu \ge 0), \\ \mathrm{e}^{\left(-\frac{-\sum(z,E)Z}{\mu}\right)}\displaystyle\int_d^z \mathrm{d}z', \dfrac{S(z', E, \mu)}{\mu}\mathrm{e}^{\left(-\frac{-\sum(z,E)z'}{\mu}\right)}, & (\mu < 0), \end{cases} \end{aligned} \tag{12}$$

where d is the thickness of the medium. After obtaining the photon flux distribution, we defined the fluence distribution of the secondary electron source and the secondary positron source by

$$\begin{cases} S_e(z, E, \mu) = \varnothing(z, E, \mu)\cdot n_{(z)} \cdot \mathrm{d}z \cdot \sigma_{\text{tot}}(z) \\ S_p(z, E, \mu) = \varnothing(z, E, \mu)\cdot n_{(z)} \cdot \mathrm{d}z \cdot \sigma_{\text{pair}}(z), \end{cases} \tag{13}$$

where $\mathrm{d}z$ is the length of the calculation unit in depth direction. The electron transport equation is given by

$$\begin{aligned} &\mu\frac{\partial N}{\partial z} + \sum_e(z)N(z, E, \mu) \\ &\quad = S_e + n_{(z)}\int_E^{\infty} \mathrm{d}E' \int_{4\pi} \mathrm{d}\Omega' N(z, E, \mu) \\ &\qquad \cdot\sigma_e(z, E', E' - E, \Omega'\cdot\Omega), \end{aligned} \tag{14}$$

where $N(z, E, \mu)$ is the differential fluence of the electron. $\sum_e(z)$ is the number of interactions between electrons and matter along a unit path at depth z. σ_e is the total cross section of electrons, including bremsstrahlung, elastic interaction, and inelastic interaction. The differential fluence distribution of electron can be obtained by the characteristic line algorithm. According to the differential

fluence distribution, the depth dose distribution of the infinitely broad beam with energy E_0 is expressed as

$$D_e(E_0,z) = \frac{n_{(z)}}{\rho_{(z)}} \int_0^{E_0} \mathrm{d}E \int_{-1}^{1} \mathrm{d}\mu \varnothing(z, E, \mu) \int_0^{\Delta E} \sigma_e(z, E, T) T \mathrm{d}T, \quad (15)$$

where ΔE is an energy parameter related to the size of the calculated voxel, indicating that energy can be deposited in the calculated voxel only when the energy transfer of the interaction is less than ΔE. $\int_0^{\Delta E} \sigma_e(z, E, T) T \mathrm{d}T$ is the electronic stopping power with energy E. In the same way, the depth dose distribution of positrons can be calculated. Therefore, the depth dose distribution of the broad photon beam in the phantom is expressed as

$$D(E_0,z) = D_e(E_0,z) + D_p(E_0,z). \quad (16)$$

As field size is small, CPE is lost resulting in vast quantities of lateral scattering, and electrons deposit energy outside the radiation field, which causes decreased radiation dose in the region of interest (ROI) and increased dose outside the ROI. The phenomenon is even more pronounced when photon beamlets are incident into lung tissue [6]. The dose distribution of secondary electrons in homogeneous tissue can be simulated by MC method, and it can be used as PBC kernel if the dose distribution is spatially invariant. The pencil beam kernel can be reused as long as radiation conditions, such as incident energy, incident direction, and voxel size, remain unchanged. In fact, the space-invariance of pencil beam kernel is affected by many variables including the heterogeneity of tissue and the irregularity of organ contour, but for bulky lung tissue, pencil beam kernel can be regarded as spatially invariant [19,20]. Thus, the study introduces a scattering factor to construct transport models of scattered photons and secondary electrons in heterogeneous media. The lung tissues in small radiation fields can be treated with laminar approximate. So, the 3D dose distribution of photon pencil beam with incident energy E in laminar lung media can be written as

$$D_p(E, x, y, z) = D_p(E, 0, 0, z) \cdot f(E, x, y, z), \quad (17)$$

where $D_p(E, x, y, z)$ is the dose at point (x, y, z) when the infinitely narrow photon pencil beam is incident at point $(0, 0, 0)$ along the $+z$ axis. $D_p(E, 0, 0, z)$ is the central axis depth dose distribution. $f(E, x, y, z)$ is the scattering factor. The 3D dose distribution is obtained by the MC method when pencil beam irradiated the pure water phantom. Then, Eq. (17) became

$$f(E, x, y, z) = D_p(E, x, y, z)/D_p(E, 0, 0, z), \quad (18)$$

where $D_p(E, x, y, z)$ is the MC pencil beam kernel and is normalized to the maximum value for convenient calculation.

For the HPBM [21–23], the heterogeneous correction of lung phantom scattering factor was mainly divided into two steps. Step one was equivalent depth correction of lung phantom scattering factor in depth direction, namely, the lung phantom scattering factor was used to approximately represent the scattering factor at equivalent depth in water. It is described as

$$\begin{cases} f'(E, x, y, z) = f(E, x, y, z_{\mathrm{eff}}) \\ z_{\mathrm{eff}} = \int_0^z \frac{\rho(h)}{\rho_w} \mathrm{d}h, \end{cases} \quad (19)$$

where $\rho(h)$ is the lung phantom density at depth h and ρ_w is the water density. z_{eff} is the equivalent depth corresponding to lung phantom depth (z). Step two was weighted density correction of lung phantom scattering factor in off-axis direction on the basis of equivalent depth correction. It is described as

$$\begin{cases} f''(E, x, y, z) = f'(E, x_{\mathrm{eff}}, y, z) \\ x_{\mathrm{eff}} = \beta \cdot \rho_{(z)} \cdot x \\ \beta = \alpha + (1 - \alpha) \cdot \rho_{(z)}, \end{cases} \quad (20)$$

where α is the scattering weight coefficient and β is the density correction coefficient. As $\rho_{(z)}$ is 1 g/cm^3, β is 1 and as $\rho_{(z)}$ is 0 g/cm^3, β is α. Moreover, the median density scattering weight coefficient was obtained by linear interpolation. x_{eff} is the equivalent off-axis distance corresponding to lung phantom off-axis distance (x) after weighted density correction. After heterogeneous correction of scattering factor, the lung phantom dose kernel is expressed as

$$D_p'(E, x, y, z) = D_p(E, 0, 0, z) \cdot f''(E, x, y, z). \quad (21)$$

In FSPB algorithm, the depth dose for infinitely broad photon beam was calculated by convolution superposition for the dose contribution of each photon pencil beam. The sum is given by

$$D(E, 0, 0, z) = \int_{-\infty}^{\infty} \mathrm{d}x \int_{-\infty}^{\infty} \mathrm{d}y \cdot D_p(E, x, y, z). \quad (22)$$

In fact, it is not necessary to integrate with respect to x or y over an infinite range and we can use a broad beam field, namely, reference radiation field. On the one hand, the lung phantom depth dose distribution at depth z was obtained by photon characteristic line algorithm in a reference radiation field and described as $D_{\mathrm{ref}}(E, 0, 0, z)$.

On the other hand, the depth dose distribution in the reference radiation field was generated by a finite number of dose kernel obtained. According to Eq. (22) we have

$$D'_{\mathrm{ref}}(E, 0, 0, z) = \int_{-a}^{a} \mathrm{d}x \int_{-b}^{b} \mathrm{d}y \cdot D'_p(E, x, y, z), \quad (23)$$

where a and b are the finite integrating ranges, and their size is related to the scattering degrees of photons and secondary electrons. Here both a and b were 10 cm. The depth distribution for pencil beam in lung phantom is redefined as

$$D''_p(E, 0, 0, z) = D_{\mathrm{ref}}(E, 0, 0, z) \cdot D_p(E, 0, 0, z)/D'_{\mathrm{ref}}(E, 0, 0, z), \quad (24)$$

and we rewrote Eq. (17) for the corrected pencil beam kernel in the form

$$D''_p(E, x, y, z) = D''_p(E, 0, 0, z) \cdot f''(E, x, y, z), \quad (25)$$

where $D''_p(E, 0, 0, z)$ is also described as the precise pencil beam kernel in laminar lung media. Since we used parallel beam, the cone beam correction coefficient was not considered. And then, with the FSPB algorithm, the dose distribution in body tissues for any radiation field can be calculated as

$$D(E, x, y, z) = \int\int \mathrm{d}x'\mathrm{d}y' I(x', y') \cdot D''_p(E, x - x', y - y', z), \quad (26)$$

where $I(x', y')$ is the incident beam energy fluence at point $(x, y, 0)$, representing the field shape. $D''_p(E, x - x', y - y', z)$ is the dose contribution of the incident beam at point (x, y, z) to the calculated point (x', y', z). Formula (26) was discretized as

$$D(E, i, j, k) = \sum_{i'}\sum_{j'} I(i', j') \cdot D''_p(E, i - i', j - j', k), \quad (27)$$

where $I(i', j')$ is the described intensity matrix with the radiation field shape. $D''_p(E, i - i', j - j', k)$ is the dose contribution of the incident beam at point (i, j, k) to the calculated point (i', j', k). X-rays used in TPS typically have a contiguous energy spectrum distribution. Therefore, the incident beam energy spectrum of 6 MV from the software Dosxyznrc was used in this research.

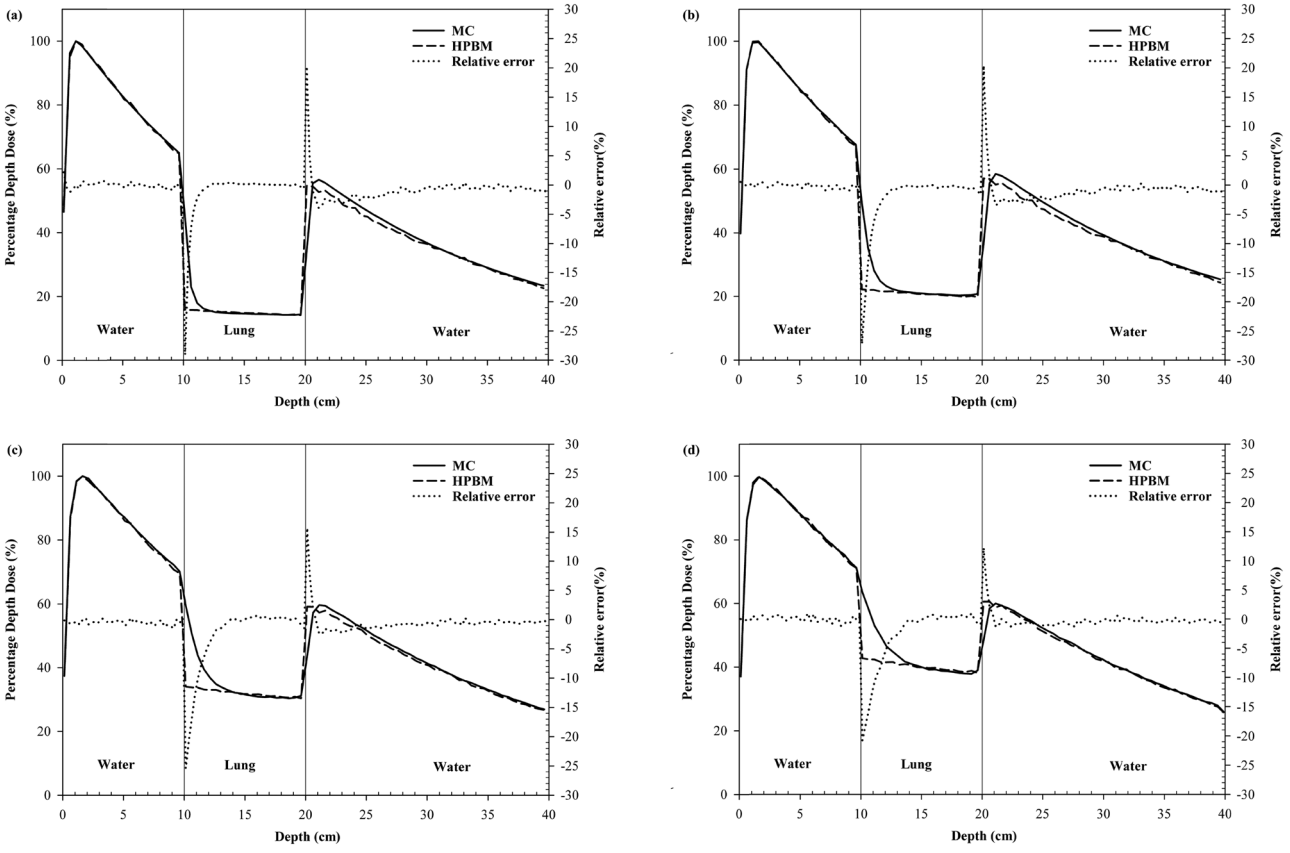

Figure 1: PDD calculated by HPBM algorithm and MC method in the lung phantom for 6 MV beam with 0.1 g/cm^3 density: (a) field size 0.5 cm × 0.5 cm, (b) field size 1 cm × 1 cm, (c) field size 2 cm × 2 cm, and (d) field size 3 cm × 3 cm.

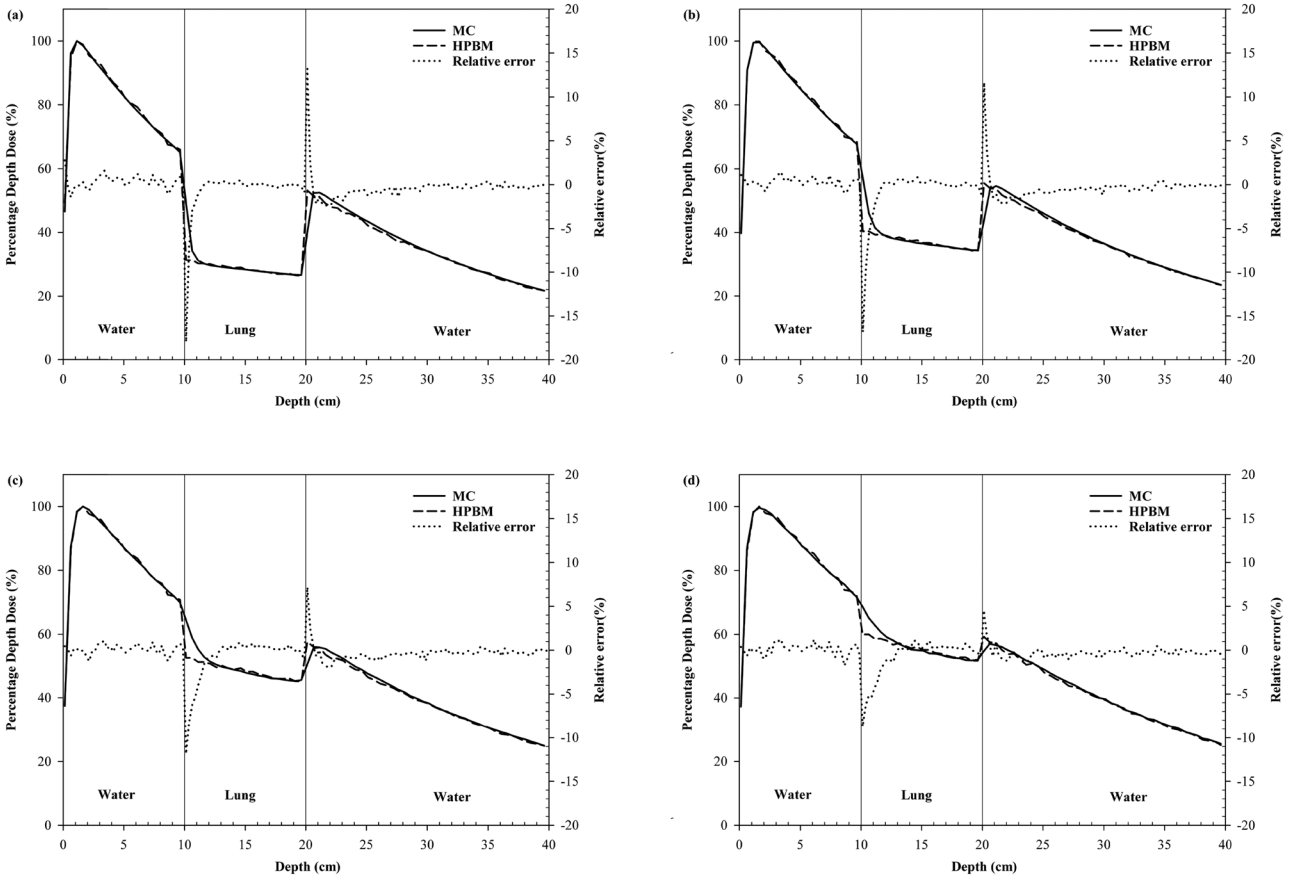

Figure 2: PDD calculated by HPBM algorithm and MC method in the lung phantom for 6 MV beam with 0.26 g/cm^3 density: (a) field size 0.5 cm × 0.5 cm, (b) field size 1 cm × 1 cm, (c) field size 2 cm × 2 cm, and (d) field size 3 cm × 3 cm.

The pencil beam kernel of pure water and lung phantoms with energy spectrum information were obtained by the MC method.

At last, in order to quantify the HPBM algorithm accuracy, the 3D dose distribution in lung phantoms calculated by HPBM algorithm was compared with the MC simulation data in small fields.

3 Results and discussion

In this study, we compare the results calculated by HPBM algorithm with MC simulation. Those results include the central axis percentage depth dose (PDD), the relative errors, and the off-axis ratio (OAR) for square, oblong, and irregular radiation fields in lung phantoms with different densities. The ratio of the difference between HPBM and MC calculated results to the maximum depth dose obtained by MC simulation is used as the relative error. We consider 6 representative small fields, namely, 0.5 cm × 0.5 cm, 1 cm × 1 cm, 2 cm × 2 cm, 3 cm × 3 cm,

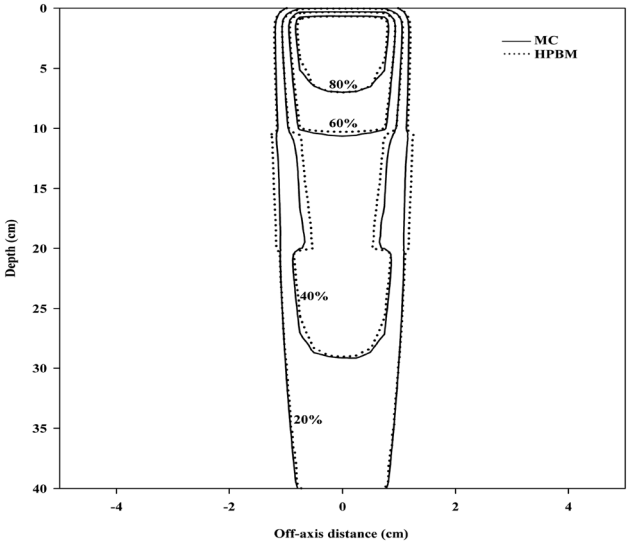

Figure 3: The dose distributions of the central plane calculated by HPBM algorithm and MC method for the field size of 2 cm × 2 cm and the lung density of 0.26 g/cm^3.

1 cm × 6 cm and the irregular field as shown in Figure 6. Here the PDD is the most concise and intuitive data for analyzing lung phantoms 3D dose distribution in small fields, while the OAR is used only for analyzing in 1 cm × 6 cm and the irregular fields.

3.1 Square fields

Figure 1(a)–(d) shows the PDD and relative error obtained by HPBM algorithm and MC method in small square fields of different sizes with 0.1 g/cm^3 lung density and photon spectrum of 6 MV. As can be seen from these figures, the depth dose distribution obtained by HPBM algorithm is basically in agreement with those obtained by MC method, but there are apparent discrepancies at different media interfaces. To be more specific, the dose calculated by HPBM algorithm is lower than MC data at the water–lung interface and lung anterior portion and higher than MC data at the second lung–water interface. However, results from the two methods coincide with each other in the middle and posterior portion of the lung. Through contrast test, the maximum error occurs in the water–lung interface. For 0.5 cm × 0.5 cm, 1 cm × 1 cm, 2 cm × 2 cm, and 3 cm × 3 cm field sizes, the maximum relative errors are 29.1, 27.2, 25.4, and 20.7%, respectively.

Figure 2(a)–(d) shows the PDD and relative error obtained by HPBM algorithm and MC method in small square fields of different sizes with 0.26 g/cm^3 density for 6 MV beam. We can see that the results have the same variation trend (Figure 1). For 0.5 cm × 0.5 cm, 1 cm × 1 cm, 2 cm × 2 cm, and 3 cm × 3 cm field sizes, the maximum relative errors are 17.9, 16.8, 11.8, and 8.7%, respectively. As an example, here we give a dose distribution of the central plane for the field with 2 cm × 2 cm and the lung density with 0.26 g/cm^3 (Figure 3).

Figure 4(a)–(d) shows the PDD and relative error obtained by HPBM algorithm and MC method in small square fields of different sizes with 0.4 g/cm^3 density for 6 MV beam. The variation trend of the PDD and

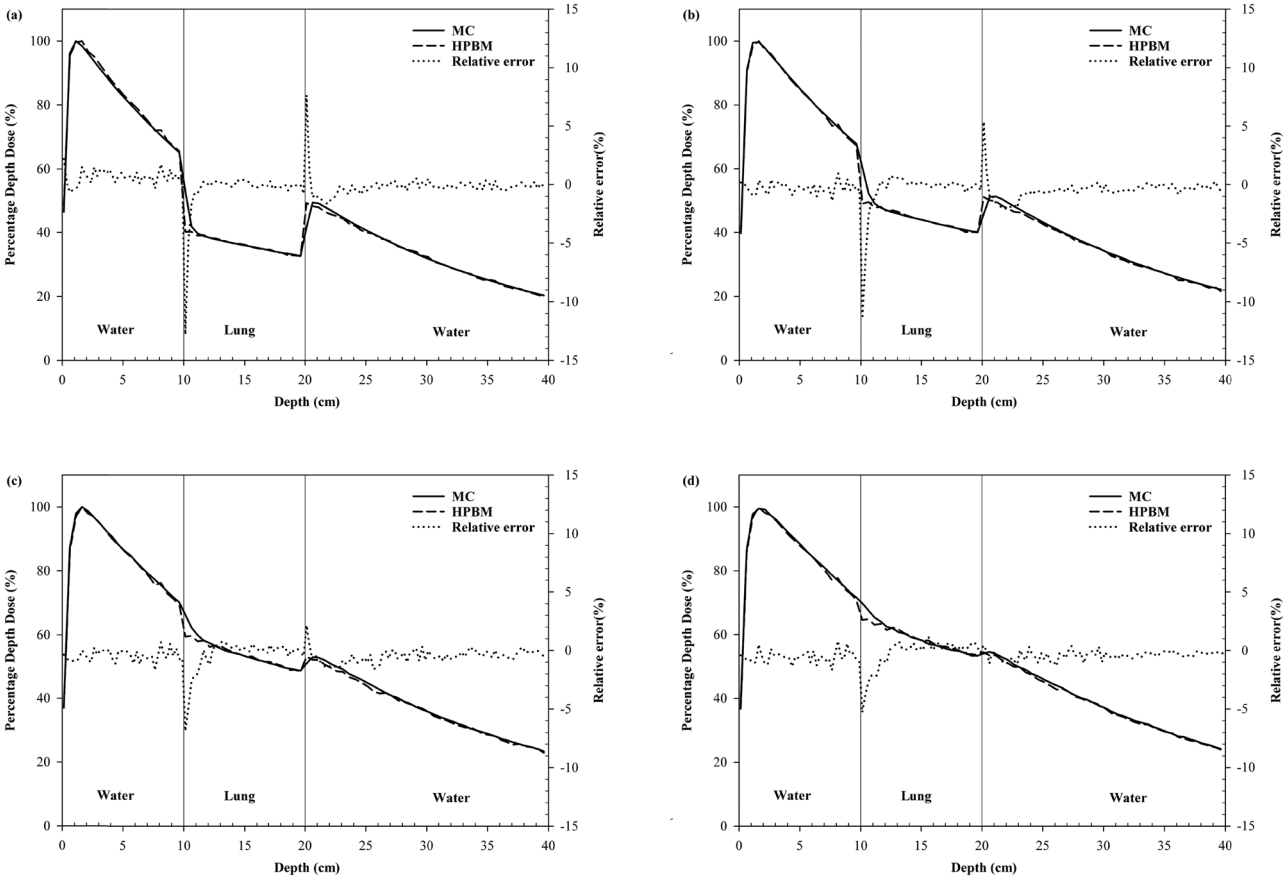

Figure 4: PDD calculated by HPBM algorithm and MC method in the lung phantom for 6 MV beam with 0.4 g/cm^3 density: (a) field size 0.5 cm × 0.5 cm, (b) field size 1 cm × 1 cm, (c) field size 2 cm × 2 cm, and (d) field size 3 cm × 3 cm.

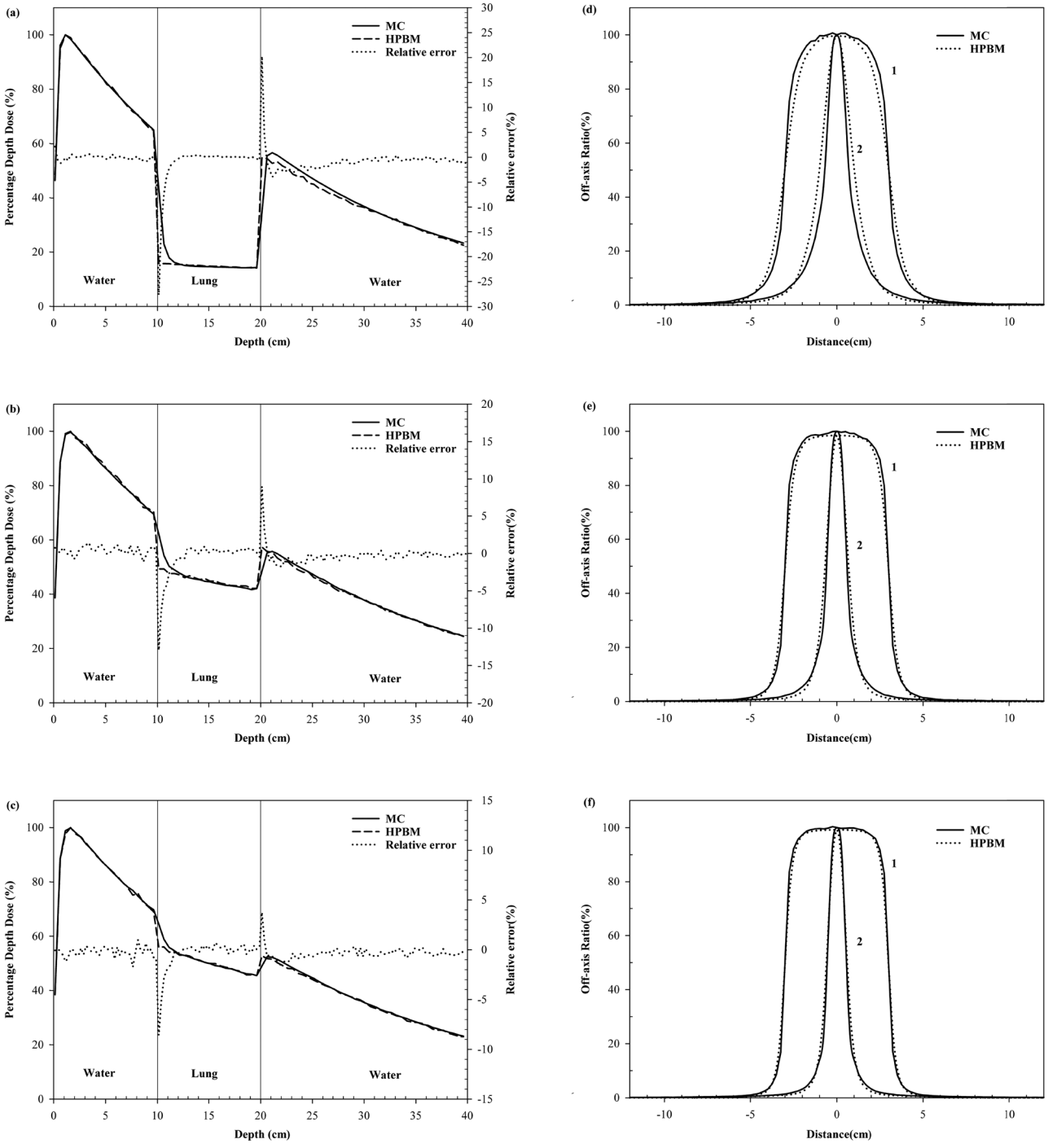

Figure 5: PDD and OAR calculated by HPBM algorithm and MC method in lung phantoms for 6 MV beam with 1 cm × 6 cm field. Numbers 1 and 2 represent OAR at 12 cm depth inside lung phantoms in the *X*-axis direction and the *Y*-axis direction, respectively. (a) PDD, density 0.1 g/cm^3, (b) PDD, density 0.26 g/cm^3, (c) PDD, density 0.4 g/cm^3, (d) OAR, density 0.1 g/cm^3, (e) OAR, density 0.26 g/cm^3, and (f) OAR, density 0.4 g/cm^3.

relative error curves are the same as that in Figures 1 and 2. For 0.5 cm × 0.5 cm, 1 cm × 1 cm, 2 cm × 2 cm, and 3 cm × 3 cm field sizes, the maximum relative errors are 12.8, 11.2, 6.9, and 5.3%, respectively. We also calculated the average error for depth doses in lung between the HPBM and MC method for the field with 1 cm × 1 cm. When the lung density is 0.1, 0.26, and 0.4 g/cm^3, the average errors are1.51, 0.92, and 0.74%, respectively.

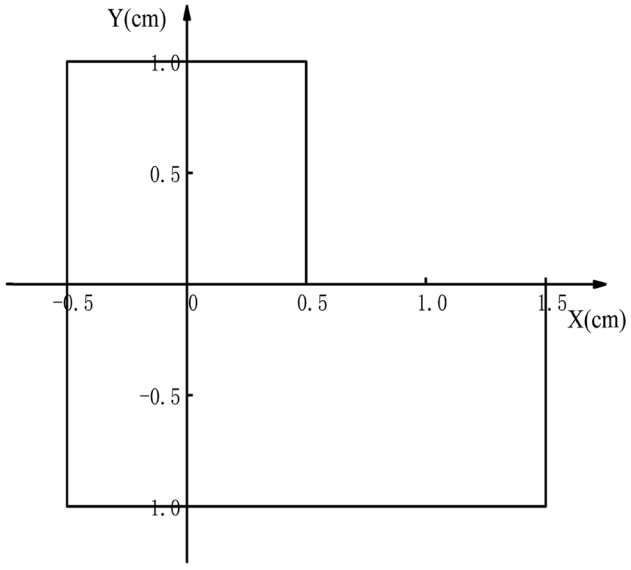

Figure 6: The size and shape of the irregular field.

3.2 Oblong field

Figure 5(a)–(c) shows the PDD and relative error of lung phantoms with different densities obtained by HPBM algorithm and MC method for 6 MV beam in 1 cm × 6 cm field. It is shown that the PDD curves obtained by the two methods agree quite well with each other, and relative errors at most depths are below 3%. But the discrepancy of central axis depth dose obtained by the two methods is obvious at media interfaces and lung anterior portion, and the maximum error occurs in the first water–lung interface. When the lung density was 0.1, 0.26, and 0.4 g/cm^3, the maximum relative errors were 27.7, 12.9, and 8.6%, respectively. Figure 5(d)–(f) shows the OAR in the *X*-axis and *Y*-axis directions for 1 cm × 6 cm field at 12 cm depth in lung phantoms. The OAR curves in the *X*-axis and *Y*-axis directions obtained by the two methods agree fairly well with each other within the irradiation field; however, the off-axis dose discrepancies between the two methods exist in the penumbra region, especially in the condition of 0.1 g/cm^3 lung density.

3.3 Irregular field

The irregular field is shown in Figure 6.

Figure 7(a)–(c) shows the PDD and relative error of lung phantoms with different densities obtained by HPBM algorithm and MC method for 6 MV beam in the irregular field. The PDD curves obtained by HPBM algorithm are in good agreement with those obtained by MC method, but the relative errors of few depths visibly increase at media interfaces and lung anterior portion, and when the lung densities are 0.1, 0.26, and 0.4 g/cm^3, the maximum relative errors, occurring in the water–lung interface, are 26.5, 13.6, and 8.3%, respectively. Figure 7(d)–(f) shows the OAR in *Y*-axis direction for the irregular field at 12 cm depth in lung phantoms. The OAR curves in *Y*-axis direction obtained by the two methods are very accordant as shown in Figure 7(d)–(f), but there are still differences in the penumbra region.

Table 1 lists the scattering weight coefficients and density correction coefficients of HPBM algorithm in lung phantoms with various radiation fields and densities. It can be seen that those coefficients decrease with the increase in the square radiation field size and lung density.

In Figures 1–5 and 7, by comparison, the main disagreement of PDD curves obtained by the two methods appears at media interfaces and lung anterior portion. Generally, the depth dose obtained by HPBM algorithm drops off faster than MC data at the water–lung interface, and rises up faster than MC data at the second lung–water interface, while the results of MC method change relatively slowly. Because the density changes intensify the effect of electronic nonequilibrium and most lateral electrons deposit energy outside the radiation field, a different dose build-up depth is needed to re-establish the CPE, which causes depth dose to decrease slowly at media interfaces [6]. However, in the middle and posterior portion of lung, the average relative errors of the two methods are less than 1% and the dose decreases steadily as the depth increases.

Furthermore, we can see clearly that the amplitude of dose dropping gradually lessens with the increase in the size of small square field at the water–lung interface, and the dose inside lung declines at nearly steady rate in the field size of 3 cm × 3 cm for 0.4 g/cm^3 lung density. Meanwhile, it can be noticed that, at media interfaces, the relative errors of the two methods decrease with the increase in the field size and lung density. The depth range in which relative errors are greater than 3% increases with the increase in the field size at lung anterior portion. As the field size increases to a certain extent, namely, the range of secondary electron is smaller than the field size, the effect of electronic nonequilibrium decreases. In this case, the tissue heterogeneous has relatively little effect of photon beam dose deposition. The amplitude of dose dropping is diminished, so the relative errors also reduced. Moreover,

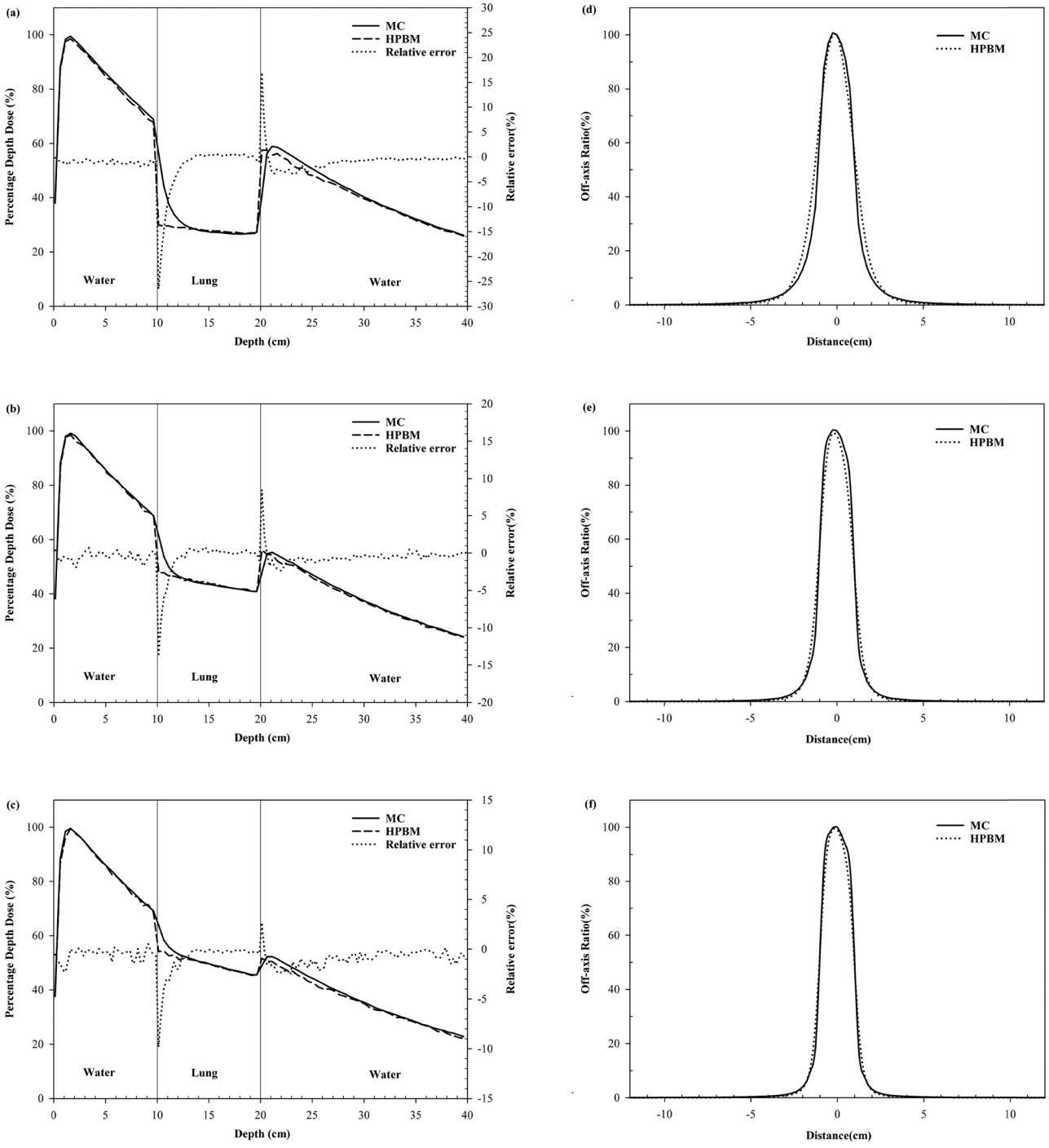

Figure 7: PDD and OAR calculated by HPBM algorithm and MC method in lung phantoms for 6 MV beam with the irregular field. (a) PDD, density 0.1 g/cm^3, (b) PDD, density 0.26 g/cm^3, (c) PDD, density 0.4 g/cm^3, (d) OAR, density 0.1 g/cm^3, (e) OAR, density 0.26 g/cm^3, and (f) OAR, density 0.4 g/cm^3.

with the increase in the lung density, the effect of electronic nonequilibrium decreases and relative errors also decrease. From the OAR curves, although the off-axis doses obtained by the two methods are slightly different in the penumbra region, the high dose deposition area is mainly in the range of radiation field, which is the same as the off-axis dose trend of the MC method.

Table 1: Scattering weight coefficients and density correction coefficients of HPBM algorithm in lung phantoms with various radiation fields and densities

Density (g/cm^3)	Field size (cm^2)	Scattering weight coefficient	Density correction coefficient
0.1	0.5 × 0.5	3.57	3.31
	1 × 1	2.75	2.58
	2 × 2	1.90	1.81
	3 × 3	1.55	1.50
	1 × 6	2.13	2.02
	Irregular field	2.17	2.05
0.26	0.5 × 0.5	2.41	2.04
	1 × 1	1.91	1.91
	2 × 2	1.29	1.21
	3 × 3	0.96	0.97
	1 × 6	1.61	1.45
	Irregular field	1.54	1.40
0.4	0.5 × 0.5	2.10	1.66
	1 × 1	0.81	1.38
	2 × 2	1.45	0.99
	3 × 3	0.86	0.82
	1 × 6	1.45	1.27
	Irregular	1.41	1.25

4 Conclusion

The high-accuracy conformal and intensity modulated radiotherapy technologies are more demanding than ever before, which promote the development of precise algorithms in small fields. However, most of the existing dose algorithms overestimate the dose of whole lung tissue, and fail to meet the accuracy of the dose algorithm. In this work, the HPBM algorithm for photon beam dose distribution with a 3D heterogeneous correction has been developed and the HPBM algorithm accuracy was verified in typical small fields for 6 MV photon beam. It can be concluded that the lung dose data obtained by HPBM algorithm are broadly in line with the MC method data: however, there are apparent discrepancies at different media interfaces. When few depths with larger relative errors at media interfaces can be ignored, the smaller the field size, the more accurate the dose was calculated by HPBM algorithm. These results show that the HPBM algorithm has potential research values for lung dose calculation in small fields. Moreover, the HPBM should be further improved for us to get a more accurate dose distribution, so as to be used in more complex cases.

Acknowledgments: The authors sincerely thank all the teachers and schoolmates who helped in the processing of this article.

Funding information: This work was supported by the National Key Research and Development Program of China (Grant no. 2016YFC0105103).

Author contributions: All authors have accepted responsibility for the entire content of this manuscript and approved its submission.

Conflict of interest: The authors state no conflict of interest.

References

[1] Mesbahi A, Dadgar H, Ghareh-Aghaji N, Mohammadzadeh M. A Monte Carlo approach to lung dose calculation in small fields used in intensity modulated radiation therapy and stereotactic body radiation therapy. J Cancer Res Ther. 2014;10(4):896–902. doi: 10.4103/0973-1482.137989.

[2] Bagheri H, Soleimani A, Gharehaghaji N, Mesbahi A, Manouchehri F, Shekarchi B, et al. An overview on small-field dosimetry in photon beam radiotherapy: Developments and challenges. J Cancer Res Ther. 2017;13(2):175–85. doi: 10.4103/0973-1482.199444.

[3] Palmans H, Andreo P, Huq MS, Seuntjens J, Christaki KE, Meghzifene A. Dosimetry of small static fields used in external photon beam radiotherapy: Summary of TRS-483, the IAEA-AAPM International Code of Practice for reference and relative dose determination. Med Phys. 2018;45:1123–45. doi: 10.1002/mp.13208.

[4] Das IJ, Francescon P, Moran JM, Ahnesjö A, Aspradakis MM, Cheng CW, et al. Report of AAPM Task Group 155: Megavoltage photon beam dosimetry in small fields and non-equilibrium conditions. Med Phys. 2021;48:886–921. doi: 10.1002/mp.15030.

[5] International Commission on Radiation Units and Measurements Report 24, determination of absorbed dose in a patient irradiated by beams of X or Gamma rays in radiotherapy procedures. Icru Report; 1976.

[6] Carrasco P, Jornet N, Duch MA, Weber L, Ginjaume M, Eudaldo T, et al. Comparison of dose calculation algorithms in phantoms with lung equivalent heterogeneities under conditions of lateral electronic disequilibrium. Med Phys. 2004;31(10):2899–911. doi: 10.1118/1.1788932.

[7] Das IJ, Ding GX, Ahnesjö A. Small fields: Nonequilibrium radiation dosimetry. Med Phys. 2008;35(1):206–15. doi: 10.1118/1.2815356.

[8] Aarup LR, Nahum AE, Zacharatou C, Juhler-Nøttrup T, Knöös T, Nyström H, et al. The effect of different lung densities on the accuracy of various radiotherapy dose calculation methods:

Implications for tumour coverage. Radiother Oncol. 2009;91(3):405–14. doi: 10.1016/j.radonc.2009.01.008.
[9] Treatment planning algorithms. Icru Rep 91. 2014;14(2):65–75. doi: 10.1093/jicru/ndx014.
[10] Papanikolaou N, Battista JJ, Boyer AL, Kappas C, Klein E, Mackie TR AAPM Report No. 85: Tissue inhomogeneity corrections for megavoltage photon beams; 2004.
[11] Reis CQM, Nicolucci P, Fortes SS, Silva LP. Effects of heterogeneities in dose distributions under nonreference conditions: Monte Carlo simulation vs dose calculation algorithms. Med Dosim. 2019;44:74–82. doi: 10.1016/j.meddos.2018.02.009.
[12] Lv XP, Zhang YB, Wu H, Yue HZ. Accuracy comparison of Acuros XB algorithm, anisotropic analytical algorithm and Monte Carlo algorithm in calculating doses of inhomogeneous tissues. Chinese J Med Phys. 2016;33(4):348–52. doi: 10.3969/j.issn.1005-202X.2016.04.005.
[13] Andreo P. Monte Carlo techniques in medical radiation physics. Phys Med Biol. 1991;36(7):861–920. doi: 10.1088/0031-9155/36/7/001.
[14] Brualla L, Rodriguez M, Lallena AM. Monte Carlo systems used for treatment planning and dose verification. Strahlenther Onkol. 2017;193:243–59. doi: 10.1007/s00066-016-1075-8.
[15] MacKie TR, Bielajew AF, Rogers D, Battista JJ. Generation of photon energy deposition kernels using the EGS Monte Carlo code. Phys Med Biol. 1988;33(1):1–20. doi: 10.1088/0031-9155/33/1/001.
[16] Mishra S, Dixit PK, Selvam TP, Yavalkar SS, Deshpande DD. Monte Carlo investigation of photon beam characteristics and its variation with incident electron beam parameters for indigenous medical linear accelerator. J Med Phys. 2018;43(1):1–8. doi: 10.4103/jmp.JMP_125_17.
[17] Luo ZM, Gou CJ, Laub W. The penetration, diffusion and energy deposition of high-energy photon. Chin phys B. 2003;12:803.
[18] Huang YC, Wu ZW, Gou CJ. The study on energy fluence for photon within radiotherapeutic energy in material. Chin J Med Phys. 2008;25(4):703–11. doi: CNKI:SUN:YXWZ.0.2008-04-003.
[19] Khan FM, Gibbons JP. Khan's The physics of radiation therapy. 5th edn. Philadelphia: Lippincott Williams & Wilki; 2014.
[20] Pawlicki T, Scanderbeg DJ, Starkschall G. Hendee's radiation therapy physics. 4th edn. Hoboken, New Jersey: John Wiley & Sons, Inc; 2016.
[21] Bourland JD, Chaney EL. A finite-size pencil beam model for photon dose calculations in three dimensions. Med Phys. 1992;19(6):1401–12. doi: 10.1118/1.596772.
[22] Dhanesar S, Darko J, Schreiner LJ. Aperture superposition dose model versus pencil beam superposition dose model for a finite size Cobalt-60 source for tomotherapy deliveries. Med Phys. 2012;39(1):206–13. doi: 10.1118/1.3665706.
[23] Zheng HQ, Sun GY, Li G, Cao R, Pei X, Hu LQ, et al. Photon dose calculation method based on Monte Carlo finite-size pencil beam model in accurate radiotherapy. Commun Comput Phys. 2013;14(5):1415–22. doi: 10.4208/cicp.221212.100413a.